

UPCommons

Portal del coneixement obert de la UPC

<http://upcommons.upc.edu/e-prints>

This document is the Accepted Manuscript version of a Published Work that appeared in final form in *ACS photonics*, copyright © American Chemical Society, after peer review and technical editing by the publisher and may be found at

<http://dx.doi.org/10.1021/acsphotonics.6b00929>

1 Monolithic CIGS–Perovskite Tandem Cell for Optimal Light 2 Harvesting without Current Matching

3 Paola Mantilla-Perez,^{*,†} Thomas Feurer,[‡] Juan-Pablo Correa-Baena,[§] Quan Liu,[†] Silvia Colodrero,[†]
4 Johann Toudert,[†] Michael Saliba,[§] Stephan Buecheler,[‡] Anders Hagfeldt,[§] Ayodhya N. Tiwari,[‡]
5 and Jordi Martorell^{†,||}

6 [†]ICFO-Institut de Ciències Fòniques, Mediterranean Technology Park, Castelldefels 08860, Spain

7 [‡]Laboratory for Thin Films and Photovoltaics, Empa-Swiss Federal Laboratories for Materials Science and Technology, Duebendorf
8 8600, Switzerland

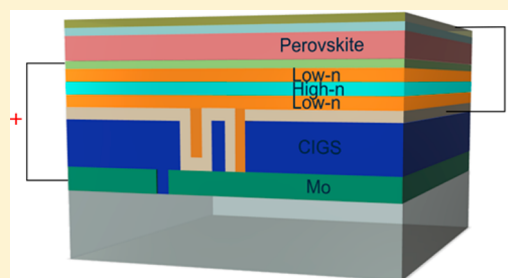
9 [§]Laboratory for Photomolecular Science, Institute of Chemical Sciences and Engineering, Ecole Polytechnique Fédérale de Lausanne,
10 Lausanne 1015, Switzerland

11 ^{||}Departament de Física, Universitat Politècnica de Catalunya, Terrassa 08222, Spain

12 **S** Supporting Information

13 **ABSTRACT:** We present a novel monolithic architecture for optimal light
14 harvesting in multijunction thin film solar cells. In the configuration we
15 consider, formed by a perovskite (PVK) cell overlying a CIGS cell, the
16 current extracted from the two different junctions is decoupled by the
17 insertion of a dielectric nonperiodic photonic multilayer structure. This
18 photonic multilayer is designed by an inverse integration approach to
19 confine the incident sunlight above the PVK band gap in the PVK absorber
20 layer, while increasing the transparency for sunlight below the PVK band
21 gap for an efficient coupling into the CIGS bottom cell. To match the
22 maximum power point voltages in a parallel connection of the PVK and
23 CIGS cells, the latter is divided into two subcells by means of a standard
24 three-laser scribing connection. Using realistic parameters for all the layers in the multijunction architecture we predict power
25 conversion efficiencies of 28%. This represents an improvement of 24% and 26% over the best CIGS and PVK single-junction
26 cells, respectively, while at the same time outperforms the corresponding current-matched standard tandem configuration by
27 more than two percentage points.

28 **KEYWORDS:** perovskite solar cells, CIGS solar cells, inverse integration, tandem, serial-parallel configuration



the corresponding single subcells,^{6,8} but the monolithic 50
character, which may be relevant to achieve a low-cost solar 51
module installation, would be lost to a large extent. A higher 52
cost associated with the connectivity complexity is expected in 53
the installation of such 4-terminal modules. On a theoretical 54
basis it was proposed to connect an indefinite number of cells 55
in each one of the branches of a parallel configuration in series 56
until the voltages of the two branches are matched.¹⁸ However, 57
no practical implementation of the device configuration was 58
considered. An alternative option proposed piling up three 59
cells, two of them in a series connection and then these two 60
connected in parallel with the remaining one.¹⁹ The latter 61
combination is an interesting proposal to match the voltage, but 62
the problem of current matching remains. 63

In this work we propose a new configuration, denoted as S-P 64
(serial-parallel), different from the standard or any other 65
tandem scheme considered until now. We describe a 66
monolithic tandem architecture where current matching 67

29 **P**erovskites (PVKs) recently emerged as a solution-
30 processed PV technology that in a short period of time
31 reached power conversion efficiencies (PCEs) comparable to
32 the ones from the well-established lower band gap crystalline Si
33 technology.^{1,2} One of the remarkable features of PVK cells is
34 their high open-circuit voltage (V_{oc}), which may reach values as
35 high as 1.24 V (at a band gap of 1.63 eV).³ Such high voltages, a
36 tunable band gap,⁴ and a high charge mobility make them an
37 optimal technology to form a pair with CIGS or crystalline Si-
38 based solar cells and lead to a low-cost multijunction
39 technology suitable for terrestrial sun energy harvesting.^{5–10}
40 In the most standard tandem configuration the two cells are in
41 a serial connection that requires current matching between
42 both cells.^{11–14} This constitutes a constraint in the optical
43 design of the optimal tandem architecture that eventually limits
44 the PCE of the final device. To partially circumvent such
45 problems, 3-terminal¹⁵ or 4-terminal^{6,13,16,17} configurations
46 have been proposed. The former one is applicable when the
47 two absorber materials are the same, while in the latter one,
48 there are no material constraints. Mechanically stacked 4-
49 terminal devices have shown efficiencies that overcome that of

Received: November 21, 2016

68 between the PVK and CIGS cells is not required. Performing
69 an optical optimization of the structure, we predict an efficiency
70 of 28% using a 1.56 eV band gap PVK and PV parameters that
71 have already been reached for the constituent CIGS or PVK
72 subcells. Furthermore, we discuss the experimental viability of
73 the proposed architecture.

74 ■ RESULTS AND DISCUSSION

75 As shown in Figure 1a, the configuration is formed with a
76 semitransparent PVK solar cell deposited on top of two CIGS

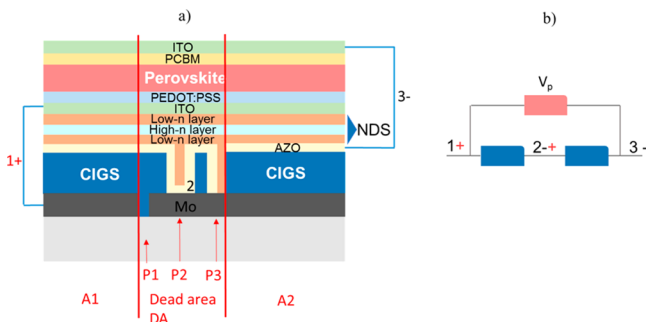


Figure 1. (a) Schematic drawing of the monolithic multijunction device composed of a two-series connected CIGS cell connected in parallel with a PVK cell. (b) Schematic drawing of the connections of the S-P configuration.

77 solar cells laterally connected in series. A schematic drawing of
78 the architecture with connection nodes numbered from 1 to 3
79 is shown in Figure 1b. Voltage matching at nodes 1 and 3 from
80 both branches of the circuit may, in principle, be achieved
81 provided the maximum power point voltage (V_{mpp}) of the light-
82 filtered CIGS cells is close to half that from the PVK cell. The
83 serial connection among the two CIGS cells can be
84 implemented by means of laser scribing, a standard technique
85 for the up-scaling of CIGS cells to modules. As seen in Figure
86 1a, a dielectric multilayer referred as a 1-D photonic
87 nonperiodic dielectric structure (NDS) is inserted on top of
88 the first CIGS solar cell serving the double purpose of avoiding
89 short-circuiting of nodes 1 and 2 and maximizing light
90 absorption for the first and second cell. On the other hand,
91 the necessary current matching between the two serial-
92 connected CIGS devices can be easily obtained by defining
93 an equal area for both.

In the implementation of the optical optimization described
94 in the Methods we consider a configuration where the CIGS
95 solar cell architecture is the standard one and some changes are
96 introduced to the PVK device, for instance, the use of top and
97 bottom transparent conductive electrodes (TEs). Specifically,
98 the S-P architecture consists of the semitransparent PVK cell on
99 top of a CIGS cell separated by the NDS as follows: glass/Mo/
100 MoSe/CIGS/CdS/i-ZnO/AZO/low- n film/high- n film/low- n
101 film/TE/PEDOT:PSS/PVK/PCBM/TE/MgF₂. As TEs for the
102 semitransparent PVK we considered 90 nm ITO films. The
103 ITO is chosen instead of the common FTO due to its better
104 processing compatibility with the underlying materials and its
105 improved near-infrared transmission. Similar thicknesses of
106 ITO films, prepared at room temperature, have been employed
107 to form a recombination layer and top contact in a monolithic
108 tandem architecture with PVK and silicon, exhibiting high fill
109 factors.¹⁰

In the S-P configuration considered here, the optical
111 optimization is performed for a device that includes the NDS
112 between the inner TE/AZO interface as seen in Figure 1a. Such
113 NDS is formed by a combination of three layers of intercalated
114 low and high refractive index materials and has a 2-fold
115 functionality. First, it electrically separates the TE anode of the
116 PVK and the AZO cathode from the CIGS, and second, it
117 confines the incident sunlight above the PVK band gap in the
118 PVK absorber layer, while increasing the transparency for
119 sunlight below the PVK band gap for an efficient coupling into
120 the CIGS bottom cell. To prevent tunnelling from electrical
121 charges between the PVK and CIGS cells, one may use MgF₂ as
122 a low- n material, which is a highly insulating transparent
123 material exhibiting a refractive index close to 1.38. For the high-
124 n film, a highly transparent dielectric material with a refractive
125 index of 2.2 would be the optimal. Possible materials for the
126 high-index layer may be TiO₂ or Si₃N₄. Considering the three
127 films, the total thickness of the NDS would be above 500 nm,
128 sufficient, in principle, to prevent electrical charge tunnelling.
129 When the inverse integration optical optimization detailed in
130 the Methods section is applied, the EQEs obtained for the
131 NDS-separated PVK and CIGS cells are shown in Figure 2a.
132 Under the assumption of a negligible extinction coefficient for
133 any of the layers within the NDS, we observe an enhancement
134 in the maximum short-circuit current of the PVK and CIGS
135 subcells, especially in the wavelength range between 700 and
136 900 nm. The NDS fine-tuning required to reach maximum
137

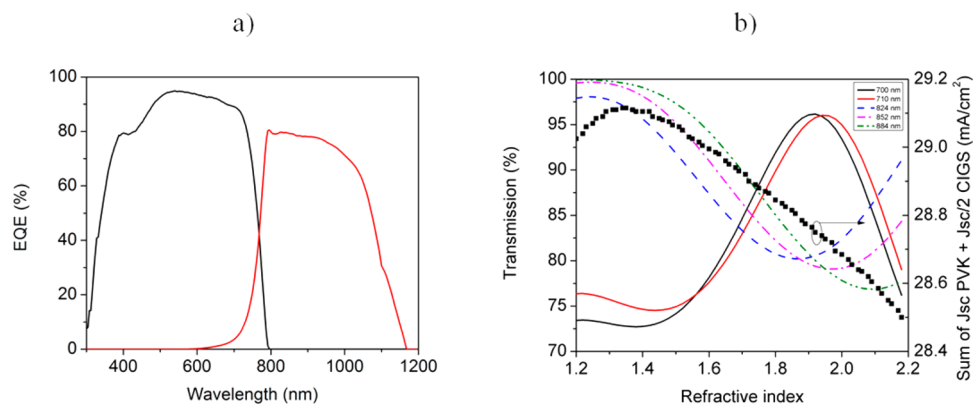


Figure 2. (a) Calculated EQE for the perovskite (black) and the CIGS (red) subcells for the optimal configuration. (b) Sum of PVK and CIGS photocurrent densities (black squares) and transmission of the NDS at 700 nm (black line), 710 nm (red), 824 nm (blue dash), 852 nm (magenta dash dot), and 884 nm (green dash dot dot) as a function of the refractive index of the low- n NDS layer.

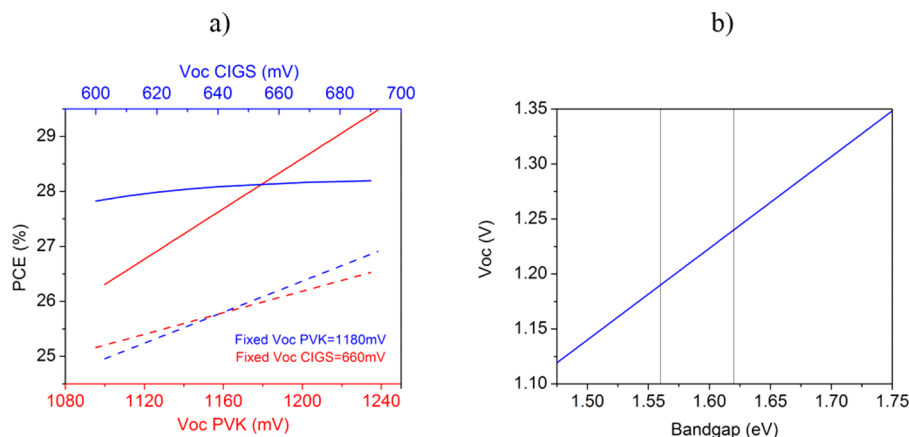


Figure 3. (a) PCEs for the tandem (dashed lines) and S-P (continuous lines) configurations. The red lines correspond to a fixed V_{oc} for the CIGS solar cells at 660 mV, while the V_{oc} of the PVK is allowed to change from 1080 to 1240 mV. The blue lines correspond to a fixed V_{oc} condition of the PVK at 1180 mV, while the V_{oc} of the CIGS is allowed to change from 600 to 690 mV. (b) Estimate of PVK V_{oc} as a function of the PVK band gap. The two reference values are marked as vertical lines.

PCE may be extracted from Figure 2b, where the transmission at five different wavelengths just above and below the PVK band gap is shown as a function of the NDS low refractive index material. In this figure one observes that for the cell architecture with the highest short-circuit current sum, when the NDS low-index material is close to 1.38, the inverse integration leads to an NDS transmission that is larger at longer wavelengths to favor absorption at the CIGS and smaller at shorter wavelengths to favor absorption in the PVK. Note that the unbalanced current density in both subcells explains why the PCE of the S-P configuration is considerably larger than the PCE for the current matched tandem, as seen in Figure 3a. The optimal thicknesses for the critical layers inside the S-P structure depend on the selected TE. When using a 90 nm indium tin oxide (ITO) film, the optimal architecture is glass/Mo/MoSe/CIGS (2.5 μm)/CdS (40 nm)/i-ZnO(50 nm)/AZO(100 nm)/low- n film (70 nm)/high- n film (220 nm)/low- n film (250 nm)/ITO (90 nm)/PEDOT:PSS (20 nm)/PVK (700 nm)/PCBM (20 nm)/ITO (90 nm)/MgF₂ (98 nm), delivering a J_{sc} of 22.06 mA/cm² for the PVK and 14.1 mA/cm² for the CIGS.

To confirm that such an increase in photocurrent in the S-P configuration corresponds to an equivalent increase in PCE, we determined the rest of the electrical parameters that characterize the overall IV curves employing the single-diode electrical equivalent circuit model. The single-diode circuit model was applied to each branch of the circuit, and then the currents were added point by point to obtain the resulting IV curve. To reach optimal PCEs, we set the fill factor (FF) between 80% and 81% for all the single-junction cells used in the S-P configuration. A similar procedure was used to determine the optimal configuration for a standard current-matched tandem, which is used as a reference for comparison. Although small variations resulting from the IV curve fitting may be found, the FF of the S-P structure closely approached that of the subcell, with the highest FF for most of the cases considered. On the other hand, the V_{oc} of the S-P is roughly limited by the voltage of the branch that has the lowest voltage, as can be seen in Figure S1 of the SI. We studied two cases, one where the V_{oc} of the PVK was fixed to 1180 mV while the V_{oc} of the CIGS was varied in the 600–700 mV range, and a second case where the V_{oc} of the CIGS was fixed to 660 mV and that of the PVK was allowed to change in the 1080–1240 mV range. The ideality

factor, series resistance, shunt resistance, and saturation current were determined to match experimental curves when available (Figure S2 of the SI) or from the computer-generated single-junction IV curves exhibiting the targeted J_{sc} , FF, and V_{oc} parameters. Note that the changes in V_{oc} considered here are not associated with band gap modifications, which will be considered below. Indeed the V_{oc} ranges encompass a wide variety of voltages that are often found in experimental CIGS or PVK single-junction devices.

As seen in Figure 3a, when a PVK cell with a V_{oc} of 1180 mV is combined with a CIGS cell in the S-P configuration, the efficiency remains more or less around 28% as the V_{oc} of the CIGS changes. This PCE is clearly larger than the PCE from any of the possible tandem configurations also shown in Figure 3a. In the event that the V_{oc} of the PVK is further increased, PCEs above 29% would be reachable, while for the standard tandem PCEs larger than 27% are, in principle, not possible. This confirms that the S-P configuration clearly outperforms the standard tandem by more than two percentage points in almost all cases. Note that, when optimal single-junction cells are considered, both configurations, tandem and S-P, will clearly outperform record PCEs for CIGS²⁰ and PVK²¹ single-junction cells.

Provided that in the S-P configuration no current matching is required between the PVK and the CIGS cells, a further increase in the PCE may be achieved by tuning the band gap of either the PVK or CIGS cells. For PVK cells several authors have considered tuning the band gap by changing the relative halide composition and observed an increase in the V_{oc} . Although in most cases studied no clear relationship was established between the V_{oc} and the band gap, from the wide band gap tuning study reported by Noh et al.⁴ one may extract a close to linear correspondence between these two parameters when the band gap is changed from 1.57 to 2.29 eV. The V_{oc} values therein reported are, however, low in comparison to recent reports. For instance, PVK cells with a measured band gap of 1.56 eV have reached a V_{oc} as high as 1.19 V.²² Similarly, for a higher band gap PVK of 1.62 eV, a V_{oc} of 1.24 eV³ was recently achieved, which corresponds to a loss in potential (difference band gap and V_{oc}) of 0.39 eV, which is close to the thermodynamic limit. Thus, an increase in V_{oc} may be achievable for the other band gaps as well once the charge extraction contacts and the perovskite composition have been

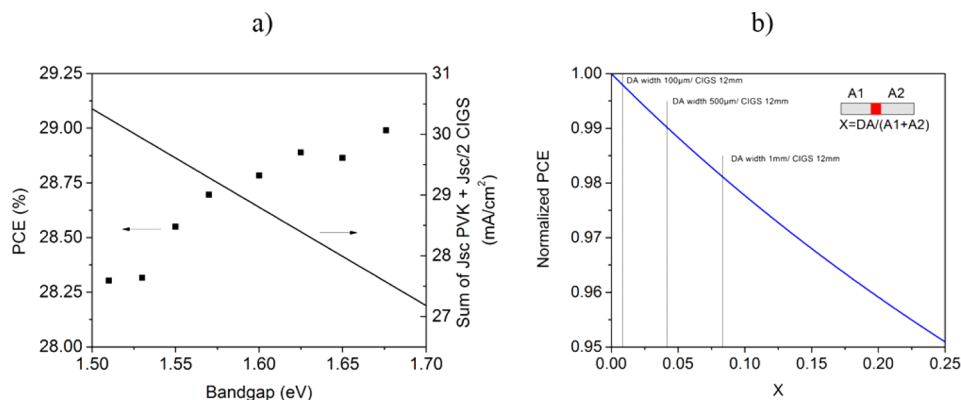


Figure 4. (a) PCE of the CIGS/PVK S-P cells as a function of the PVK band gap (squares) and sum of PVK and CIGS halved short-circuit current densities for the S-P configuration as a function of the PVK band gap (line). (b) PCE as a function of DA width of the serial-connected cells assuming devices with an area of $12 \times 12 \text{ mm}^2$.

224 optimized to overcome limiting effects such as the one
 225 described in ref 23. For this work, the above two values are
 226 taken as references and used to establish a linear relation
 227 between the V_{oc} and the band gap in the range of 1.51 to 1.71
 228 eV, shown in Figure 3b. At present, there are material
 229 compositions for PVK cells yielding band gaps below 1.56
 230 eV.^{13,24,25} However, such compositions have led to suboptimal
 231 devices, which were not taken as references for this analysis. A
 232 monotonic decrease of the total calculated short-circuit current
 233 density as the band gap increases is observed in Figure 4a. Note
 234 that we have plotted the sum of the short-circuit current density
 235 of the PVK with half of the CIGS to account for the differences
 236 in area inherent to the S-P structure. When estimating the PCE
 237 using the same single-diode model described above, one
 238 observes, as can be seen in Figure 4a, an increase in PCE as the
 239 band gap of the PVK increases. Although this may seem
 240 counterintuitive provided the band gap of PVK is well above
 241 the optimal single-junction solar cell band gap, the explanation
 242 is that the band gap increase implies a better voltage matching
 243 with the CIGS branch of the circuit.

244 ■ METHODS

245 **Intercalated Nonperiodic Photonic Structure for**
 246 **Optimal Light Harvesting.** To design the specific
 247 architecture for the S-P cell, we set the sum of the
 248 photocurrents as the target optimization parameter within our
 249 numerical calculations.

250 From Figure 1b, it can be seen that the maximum electrical
 251 power P derived from the device is given by

$$252 \quad P = (I_{\text{CIGS}} + I_{\text{PVK}})V_p \times \text{FF} \quad (1)$$

253 ,where I_{CIGS} is the short-circuit current generated by the CIGS
 254 solar cell and I_{PVK} is the short-circuit current generated by the
 255 PVK. V_p and FF are the corresponding voltage and fill factor
 256 from the parallel connection.

$$257 \quad I_{\text{PVK}} = J_{\text{PVK}}(A_T) \quad (2)$$

258 with J_{PVK} being the short-circuit current density from the PVK
 259 and A_T the total illumination area of the device. Neglecting the
 260 dead area, A_T corresponds to

$$261 \quad A_T = A_1 + A_2 \quad (3)$$

where A_1 and A_2 are the areas for the CIGS subcells (for
 262 practical considerations refer to the next subsection). The
 263 current flowing through the CIGS cells must fulfill
 264

$$I_{\text{CIGS}} = A_1 J_{\text{CIGS1}} = A_2 J_{\text{CIGS2}} \quad (4)$$

By simple algebra one may write the PCE as
 266

$$\text{PCE} = \frac{[(A_1 J_{\text{CIGS1}}) + (A_2 J_{\text{PVK}})]V_p \times \text{FF}}{P_{\text{AM1.5T}}} \quad (5)$$

We determine the optimal cell architecture by implementing an
 268 inverse integration approach where the photocurrent from each
 269 one of a large set of possible configuration solutions is
 270 numerically computed using a transfer matrix formalism.
 271 Configurations are defined by a large set of different input
 272 parameters, including thicknesses and/or optical constants for
 273 some or all the device layers, which are allowed to vary within a
 274 specified range. The target solution is selected from that set of
 275 all possible solutions.
 276

When implementing the transfer matrix model, it is assumed
 277 that all layers are considered homogeneous and isotropic, such
 278 that their optical characteristics can be represented by scalar
 279 complex indexes of refraction; interfaces between adjacent
 280 layers are parallel and optically flat; incident light is
 281 perpendicular to the stack and can be described by plane
 282 waves; and the efficiencies in exciton diffusion, charge
 283 separation, and carrier transport and collection are wavelength
 284 independent. To perform these calculations, one must know
 285 the complex index of refraction and thickness for each layer in
 286 the architecture. The refractive indexes for each layer were
 287 taken from refs 26 and 27 for the CIGS solar cell and from refs
 288 28 and 29 for most of the layers in the PVK solar cell.
 289

Using the calculated electric field intensities for the CIGS
 290 and PVK, together with their optical properties, the absorption
 291 is computed to finally determine the short-circuit current
 292 density (J_{sc}) for each subcell. J_{sc} 's for the PVK and CIGS cells
 293 were computed for 10 000 different combinations of layer
 294 thicknesses when varying the absorber layers, the entrance
 295 transparent electrode, and the intermediate dielectric NDS
 296 layers. The thickness ranges were in accordance with the
 297 experimental constraints to obtain an optimal FF or V_{oc} for
 298 both cells. We assumed an internal quantum efficiency (IQE)
 299 of 100% for the PVK cell, as demonstrated in refs 30 and 31
 300 and 92% for the CIGS solar cells.³² In the PCE estimates, we
 301 obtained the equivalent parallel voltage V_p and FF by adding
 302

303 the *IV* curves corresponding to each one of the branches of the
304 circuit.

305 **Experimental Implementation of S-P Structure.** The
306 CIGS bottom cells in this design can be deposited in the
307 different ways described in the literature, since there are no
308 special limitations on process temperature or conditions
309 present at this point. In order to reach the desired efficiency,
310 a deposition by co-evaporation or precursor selenization seems
311 to be favorable. The substrate can be rigid (soda lime glass) or
312 flexible (polyimides, steel), especially in view of possible roll-to-
313 roll production. The back contact is typically Mo around 500
314 nm. The absorber will be between 2 and 3 μm thick, followed
315 by a buffer layer (most likely CdS by chemical bath deposition)
316 and a multilayer of intrinsic and doped zinc oxide as TE. The
317 front contact sheet resistance should be below 10 ohm/sq for a
318 monolithic cell interconnection.

319 Concerning the fabrication of the PVK device on top of the
320 CIGS, a number of constraints are introduced to prevent
321 damage of the bottom CIGS layer. For instance, thermal
322 instability has been observed for the n-type buffer layer in CIGS
323 solar cells, where atoms tend to diffuse from the buffer to the
324 absorber layer, significantly reducing the performance of the
325 device by an augmented recombination. Temperatures above
326 300 $^{\circ}\text{C}$ trigger this process and have been shown to be
327 detrimental to all PV parameters of CIGS solar cells.³³
328 Therefore, annealing processes used to manufacture all the
329 layers within the PVK device are temperature-limited, which
330 excludes the use of frequent configurations such as the
331 mesoscopic PVK on 500 $^{\circ}\text{C}$ sintered TiO_2 . The PVK layer
332 itself does not require high-temperature annealing and neither
333 does the PCBM. On the other hand, ITO has been shown to
334 provide good-quality transparent electrodes at the bottom or
335 the top of PVK solar cells.^{10,34} Connection of PVK cells to
336 modules has been reported in the literature,³⁵ some with a
337 reduced area loss of 3% of the total 16 cm^2 module area.³⁶

338 Similarly to the case of PVK, for the lateral serial connection
339 of the CIGS solar cells three structured patterns denominated
340 P1, P2, and P3 are required, as seen in Figure 1a. The first
341 pattern, P1, and the third pattern, P3, separate the positive and
342 negative contacts of adjacent cells, respectively. The second
343 pattern, P2, allows the negative contact of one cell to be
344 connected with the positive contact of the following cell. The
345 region in between P1 and P3, including both, is the dead area
346 (DA). Typically, laser scribing is employed to define such
347 patterns. If we assume that the dead area corresponds to a
348 fraction X of the total CIGS active cell area, then

$$349 \quad \text{DA} = X(A_1 + A_2) \quad (6)$$

350 Within the optically optimized S-P structure we consider the
351 effect of the DA in the total PCE by normalizing it without
352 neglecting the DA. As can be seen in Figure 4b, under the
353 assumption of a cell larger than 1 cm, the effective loss in PCE
354 is less than 2% even when the separation between P1 and P3,
355 including the width of such laser cuts, is as large as 500 μm . For
356 separations as small as 100 μm , which have been recently
357 outperformed in the series connection of CIGS cells,³⁷ the loss
358 in PCE is negligible.

359 ■ CONCLUSIONS

360 In summary, we proposed and studied a new tandem
361 configuration where the constraint of current density matching
362 is removed. Two CIGS cells laterally connected in series may
363 be connected in parallel with a PVK cell matching the

maximum power point voltages. The configuration studied is 364
monolithic, but the currents from the top PVK and the bottom 365
CIGS cells can be extracted separately. We demonstrated that 366
when the two cells are electrically separated by a dielectric 367
nonperiodic photonic multilayer structure, such photonic 368
structure can be designed to effectively confine the incident 369
sun light above the PVK band gap in the PVK absorber layer. 370
The same photonic structure is used to reach an optimal 371
transparency for sunlight below this band gap and efficiently 372
couple it into the CIGS bottom cell. Using realistic current 373
state-of-the-art parameters for all layers in the multijunction 374
architecture we estimated that PCEs above 28% can be 375
achieved. The PCE of the S-P configuration is for most of the 376
cases studied two percentage points higher in efficiency than 377
that estimated for an optimal series-connected standard tandem 378
configuration or 22.6% and 22.1%, which are the maximum 379
efficiencies reported for CIGS and PVK single-junction cells, 380
respectively. Any improvement in the subcells will further 381
increase the potential efficiency of the S-P cell. For a successful 382
experimental implementation of the S-P configuration, the 383
procedures to fabricate high-quality semitransparent electrodes 384
with the limitations imposed by the layers already deposited 385
must be improved. In addition, the optical optimization of the 386
NDS must be made compatible with its role of preventing 387
short-circuiting between the two subcells. 388

■ ASSOCIATED CONTENT

📄 Supporting Information

The Supporting Information is available free of charge on the
ACS Publications website at DOI: 10.1021/acspphoto-
nics.6b00929.

Curve of equivalent V_{oc} for the S-P configuration when
varying the V_{oc} of the PVK subcell or V_{oc} of the CIGS
subcell; fitting data of *IV* curves; module interconnection
schemes for the S-P configuration (PDF)

■ AUTHOR INFORMATION

Corresponding Author

*E-mail: paola.mantilla@icfo.es.

ORCID

Paola Mantilla-Perez: 0000-0003-4801-4949

Juan-Pablo Correa-Baena: 0000-0002-3860-1149

Johann Toudert: 0000-0002-1609-1934

Notes

The authors declare no competing financial interest.

■ ACKNOWLEDGMENTS

P.M.P., Q.L., S.C., J.T., and J.M. acknowledge financial support
from the Spanish MINECO (Severo Ochoa program, grant no.
SEV-2015-0522), the MINECO, the Fondo Europeo de
Desarrollo Regional FEDER (grant no. MAT2014-52985-R),
the Fundació Privada Cellex, and the EC FP7 Program (ICT-
2011.35) under grant agreement no. NMP3-SL-2013-604506.
M.S. acknowledges support from the cofunded Marie
Sklodowska Curie fellowship, H2020 grant agreement no.
665667. Financial funding from the Swiss National Science
Foundation (SNF)-NanoTera as well as Competence Center
for Energy and Mobility (CCEM Connect-PV) is gratefully
acknowledged.

420 ■ REFERENCES

- 421 (1) Battaglia, C.; Cuevas, A.; De Wolf, S. High-Efficiency Crystalline
422 Silicon Solar Cells: Status and Perspectives. *Energy Environ. Sci.* **2016**,
423 *9*, 1552–1576.
- 424 (2) Saliba, M.; Matsui, T.; Seo, J.; Domanski, K.; Correa-Baena, J.;
425 Nazeeruddin, M.; Zakeeruddin, S.; Tress, W.; Abate, A.; Hagfeldt, A.;
426 Grätzel, M. Cesium-Containing Triple Cation Perovskite Solar Cells:
427 Improved Stability, Reproducibility and High Efficiency. *Energy*
428 *Environ. Sci.* **2016**, *9*, 1989–1997.
- 429 (3) Saliba, M.; Matsui, T.; Domanski, K.; Seo, J.; Ummadisingu, A.;
430 Zakeeruddin, S.; Correa-Baena, J.; Tress, W.; Abate, A.; Hagfeldt, A.;
431 Grätzel, M. Incorporation of Rubidium Cations into Perovskite Solar
432 Cells Improves Photovoltaic Performance. *Science* **2016**, *354*, 206–
433 209.
- 434 (4) Noh, J.; Im, S.; Heo, J.; Mandal, T.; Seok, S. Chemical
435 Management for Colorful, Efficient, and Stable Inorganic–Organic
436 Hybrid Nanostructured Solar Cells. *Nano Lett.* **2013**, *13*, 1764–1769.
- 437 (5) Todorov, T.; Gershon, T.; Gunawan, O.; Lee, Y.; Sturdevant, C.;
438 Chang, L.; Guha, S. Monolithic Perovskite-CIGS Tandem Solar Cells
439 Via In Situ Bandgap Engineering. *Adv. Energy Mater.* **2015**, *5*, 1500799.
- 440 (6) Kranz, L.; Abate, A.; Feurer, T.; Fu, F.; Avancini, E.; Löckinger, J.;
441 Reinhard, P.; Zakeeruddin, S.; Grätzel, M.; Buecheler, S.; Tiwari, A.
442 High-Efficiency Polycrystalline Thin Film Tandem Solar Cells. *J. Phys.*
443 *Chem. Lett.* **2015**, *6*, 2676–2681.
- 444 (7) McMeekin, D.; Sadoughi, G.; Rehman, W.; Eperon, G.; Saliba,
445 M.; Horantner, M.; Haghighirad, A.; Sakai, N.; Korte, L.; Rech, B.;
446 Johnston, M. B.; Herz, L. M.; Snaith, H. J. A Mixed-Cation Lead
447 Mixed-Halide Perovskite Absorber for Tandem Solar Cells. *Science*
448 **2016**, *351*, 151–155.
- 449 (8) Bailie, C.; Christoforo, M.; Mailoa, J.; Bowring, A.; Unger, E.;
450 Nguyen, W.; Burschka, J.; Pellet, N.; Lee, J.; Grätzel, M.; Noufi, R.;
451 Buonassisi, T.; Salleo, A.; McGehee, M. D. Semi-Transparent
452 Perovskite Solar Cells for Tandems with Silicon and CIGS. *Energy*
453 *Environ. Sci.* **2015**, *8*, 956–963.
- 454 (9) Mailoa, J.; Bailie, C.; Johlin, E.; Hoke, E.; Akey, A.; Nguyen, W.;
455 McGehee, M.; Buonassisi, T. A. 2-Terminal Perovskite/Silicon
456 Multijunction Solar Cell Enabled by a Silicon Tunnel Junction. *Appl.*
457 *Phys. Lett.* **2015**, *106*, 121105.
- 458 (10) Albrecht, S.; Saliba, M.; Correa Baena, J.; Lang, F.; Kegelmann,
459 L.; Mews, M.; Steier, L.; Abate, A.; Rappich, J.; Korte, L.; Schlattmann,
460 R.; Nazeeruddin, M. K.; Hagfeldt, A.; Grätzel, M.; Rech, B. Monolithic
461 Perovskite/Silicon-Heterojunction Tandem Solar Cells Processed at
462 Low Temperature. *Energy Environ. Sci.* **2016**, *9*, 81–88.
- 463 (11) Todorov, T.; Gershon, T.; Gunawan, O.; Sturdevant, C.; Guha,
464 S. Perovskite-Kesterite Monolithic Tandem Solar Cells with High
465 Open-Circuit Voltage. *Appl. Phys. Lett.* **2014**, *105*, 173902.
- 466 (12) Reinhard, M.; Sonntag, P.; Eckstein, R.; Bürkert, L.; Bauer, A.;
467 Dimmler, B.; Lemmer, U.; Colsmann, A. Monolithic Hybrid Tandem
468 Solar Cells Comprising Copper Indium Gallium Diselenide and
469 Organic Sub-cells. *Appl. Phys. Lett.* **2013**, *103*, 143904.
- 470 (13) Eperon, G.; Leijtens, T.; Bush, K.; Prasanna, R.; Green, T.;
471 Wang, J.; McMeekin, D.; Volonakis, G.; Milot, R.; May, R.; Palmstrom,
472 A.; Slotcavage, D. J.; Belisle, R. A.; Patel, J. B.; Parrott, E. S.; Sutton, R.
473 J.; Ma, W.; Moghadam, F.; Conings, B.; Babayigit, A.; Boyen, H.-G.;
474 Bent, Stacey; Giustino, F.; Herz, L. M.; Johnston, M. B.; McGehee, M.
475 D.; Snaith, H. J. Perovskite-Perovskite Tandem Photovoltaics with
476 Optimized Bandgaps. *Science* **2016**, *354*, 861.
- 477 (14) Chae, S.; Park, S.; Joo, O.; Jun, Y.; Min, B.; Hwang, Y. Highly
478 Stable Tandem Solar Cell Monolithically Integrating Dye-Sensitized
479 and CIGS Solar Cells. *Sci. Rep.* **2016**, *6*, 30868.
- 480 (15) Sista, S.; Hong, Z.; Park, M.; Xu, Z.; Yang, Y. High-Efficiency
481 Polymer Tandem Solar Cells With Three-Terminal Structure. *Adv.*
482 *Mater.* **2010**, *22*, E77–E80.
- 483 (16) Löper, P.; Moon, S.; Martín de Nicolas, S.; Niesen, B.; Ledinsky,
484 M.; Nicolay, S.; Bailat, J.; Yum, J.; De Wolf, S.; Ballif, C. Organic–
485 Inorganic Halide Perovskite/Crystalline Silicon Four-Terminal
486 Tandem Solar Cells. *Phys. Chem. Chem. Phys.* **2015**, *17*, 1619–1629.
- 487 (17) Fu, F.; Feurer, T.; Jäger, T.; Avancini, E.; Bissig, B.; Yoon, S.;
488 Buecheler, S.; Tiwari, A. Low-Temperature-Processed Efficient Semi-
Transparent Planar Perovskite Solar Cells For Bifacial and Tandem
Applications. *Nat. Commun.* **2015**, *6*, 8932.
- (18) Strandberg, R. Detailed Balance Analysis of Area De-Coupled
Double Tandem Photovoltaic Modules. *Appl. Phys. Lett.* **2015**, *106*,
033902.
- (19) Guo, F.; Li, N.; Fecher, F.; Gasparini, N.; Quiroz, C.;
Bronnbauer, C.; Hou, Y.; Radmilović, V.; Radmilović, V.; Spiecker,
E.; Forberich, K.; Brabec, C. J. A Generic Concept to Overcome
Bandgap Limitations for Designing Highly Efficient Multi-Junction
Photovoltaic Cells. *Nat. Commun.* **2015**, *6*, 7730.
- (20) Jackson, P.; Wuerz, R.; Hariskos, D.; Lotter, E.; Witte, W.;
Powalla, M. Effects of Heavy Alkali Elements in Cu(In,Ga)Se₂ Solar
Cells with Efficiencies up to 22.6%. *Phys. Status Solidi RRL* **2016**, *10*,
583–586.
- (21) National Renewable Energy Laboratory, Best Research-Cell
Efficiencies chart; www.nrel.gov/ncpv/images/efficiency_chart.jpg.
- (22) Correa Baena, J.; Steier, L.; Tress, W.; Saliba, M.; Neutzner, S.;
Matsui, T.; Giordano, F.; Jacobsson, T.; Srimath Kandada, A.;
Zakeeruddin, S.; Petrozza, A.; Abate, A.; Nazeeruddin, M. K.;
Grätzel, M.; Hagfeldt, A. Highly Efficient Planar Perovskite Solar
Cells Through Band Alignment Engineering. *Energy Environ. Sci.* **2015**,
8, 2928–2934.
- (23) Slotcavage, D.; Karunadasa, H.; McGehee, M. Light-Induced
Phase Segregation in Halide-Perovskite Absorbers. *ACS Energy Lett.*
2016, *1*, 1199–1205.
- (24) Filip, M.; Eperon, G.; Snaith, H.; Giustino, F. Steric Engineering
of Metal-Halide Perovskites with Tunable Optical Bandgaps. *Nat.*
Commun. **2014**, *5*, 5757.
- (25) Yang, Z.; Rajagopal, A.; Chueh, C.; Jo, S.; Liu, B.; Zhao, T.; Jen,
A. Stable Low-Bandgap Pb-Sn Binary Perovskites for Tandem Solar
Cells. *Adv. Mater.* **2016**, *28*, 8990–8997.
- (26) Hara, T.; Maekawa, T.; Minoura, S.; Sago, Y.; Niki, S.; Fujiwara,
H. Quantitative Assessment of Optical Gain and Loss in Submicron-
Textured CuIn_(1-x)Ga_xSe₂ Solar Cells Fabricated by Three-Stage
Coevaporation. *Phys. Rev. Appl.* **2014**, *2*, 10.1103/PhysRevAp-
plied.2.034012
- (27) Macco, B.; Wu, Y.; Vanhemel, D.; Kessels, W. High Mobility
In₂O₃:H Transparent Conductive Oxides Prepared by Atomic Layer
Deposition and Solid Phase Crystallization. *Phys. Status Solidi RRL*
2014, *8*, 987–990.
- (28) Correa-Baena, J.; Anaya, M.; Lozano, G.; Tress, W.; Domanski,
K.; Saliba, M.; Matsui, T.; Jacobsson, T. J.; Calvo, M. E.; Abate, A.;
Grätzel, M.; Míguez, H.; Hagfeldt, A. Unbroken Perovskite: Interplay
of Morphology, Electrooptical Properties, and Ionic Movement. *Adv.*
Mater. **2016**, *28*, 5031–5037.
- (29) Chen, C.; Hsiao, S.; Chen, C.; Kang, H.; Huang, Z.; Lin, H.
Optical Properties of Organometal Halide Perovskite Thin Films and
General Device Structure Design Rules for Perovskite Single and
Tandem Solar Cells. *J. Mater. Chem. A* **2015**, *3*, 9152–9159.
- (30) Yang, B.; Dyck, O.; Poplawsky, J.; Keum, J.; Puzosky, A.; Das,
S.; Ivanov, I.; Rouleau, C.; Duscher, G.; Geohagan, D.; Xiao, K.
Perovskite Solar Cells with Near 100% Internal Quantum Efficiency
Based on Large Single Crystalline Grains and Vertical Bulk
Heterojunctions. *J. Am. Chem. Soc.* **2015**, *137*, 9210–9213.
- (31) Lin, Q.; Armin, A.; Nagiri, R.; Burn, P.; Meredith, P. Electro-
Optics of Perovskite Solar Cells. *Nat. Photonics* **2014**, *9*, 106–112.
- (32) Pettersson, J.; Torndahl, T.; Platzer-Björkman, C.; Hulqvist, A.;
Edoff, M. The Influence of Absorber Thickness on Cu(In, Ga)Se₂
Solar Cells with Different Buffer Layers. *IEEE J. Photovolt.* **2013**, *3*, 3.
- (33) Wi, J.; Kim, T.; Kim, J.; Lee, W.; Cho, D.; Han, W.; Chung, Y.
Photovoltaic Performance and Interface Behaviors of Cu(In,Ga)Se₂
Solar Cells With a Sputtered-Zn(O,S) Buffer Layer by High-
Temperature Annealing. *ACS Appl. Mater. Interfaces* **2015**, *7*,
17425–17432.
- (34) Duong, T.; Lal, N.; Grant, D.; Jacobs, D.; Zheng, P.; Rahman,
S.; Shen, H.; Stocks, M.; Blakers, A.; Weber, K.; White, T. P.;
Catchpole, K. R. Semitransparent Perovskite Solar Cell with Sputtered
Front and Rear Electrodes for a Four-Terminal Tandem. *IEEE J.*
Photovolt. **2016**, *6*, 679–687.

- 558 (35) Fakhruddin, A.; Di Giacomo, F.; Palma, A.; Matteocci, F.;
559 Ahmed, I.; Razza, S.; D'Epifanio, A.; Licoccia, S.; Ismail, J.; Di Carlo,
560 A.; Brown, T. M.; Jose, R. Vertical TiO₂ Nanorods as a Medium for
561 Stable and High-Efficiency Perovskite Solar Modules. *ACS Nano* **2015**,
562 *9*, 8420–8429.
- 563 (36) Gehlhaar, R.; Merckx, T.; Masse de la Huerta, C.; Qiu, W.;
564 Cheyins, D.; Aernouts, T. Perovskite Solar Modules with Minimal Area
565 Loss Interconnections. *SPIE Newsroom* **2015**, *2/3* [10.1117/
566 2.1201509.006116](https://doi.org/10.1117/2.1201509.006116).
- 567 (37) Nishiwaki, S.; Burn, A.; Buecheler, S.; Muralt, M.; Pilz, S.;
568 Romano, V.; Witte, R.; Krainer, L.; Spühler, G.; Tiwari, A. A
569 Monolithically Integrated High-Efficiency Cu(In,Ga)Se₂ Mini-Module
570 Structured Solely by Laser. *Prog. Photovoltaics* **2015**, *23*, 1908–1915.